Chemical Engineering Journal 513 (2025) 162835

Contents lists available at ScienceDirect

Chemical Engineering Journal

journal homepage: www.elsevier.com/locate/cej

Conductive metal-organic framework@fiber composites constructed sunlight-driven actuators with self-powered sensing function for internet of things applications

Yongqiang Qian [a,b,c,1], Wanyi Cheng [a,c,1], Gang Xu [d,e], Guan-E Wang [d,*], Luzhuo Chen [a,c,*]

[a] Fujian Provincial Key Laboratory of Quantum Manipulation and New Energy Materials, College of Physics and Energy, Fujian Normal University, Fuzhou 350117, China
[b] Fujian Laser Precision Machining Engineering Technology Research Center, School of Mechanical and Electrical, Information Engineering, Putian University, Putian 351100, China
[c] Fujian Provincial Collaborative Innovation Center for Advanced High-Field Superconducting Materials and Engineering, Fuzhou 350117, China
[d] State Key Laboratory of Structural Chemistry, Fujian Institute of Research on the Structure of Matter, Chinese Academy of Sciences (CAS), Fuzhou 350117, China
[e] Fujian Science & Technology Innovation Laboratory for Optoelectronic Information of China, Fuzhou 350108, China

ARTICLE INFO

Keywords:
Actuator
Conductive metal–organic framework
Photo-thermoelectric
Generator
Internet of things

ABSTRACT

Rapid advancement of Internet of Things technology propels novel actuators towards independence, autonomy and intelligence. Self-powered actuators, which are highly integrated and require no external power supply, have garnered extensive interest. However, current actuating systems are deficient in recognition and feedback of sensing signals, restricting their intelligence. Herein, we report sunlight-driven self-powered actuators and intelligent systems based on conductive metal–organic framework@fiber composites. The inherent π-conjugated electron system of $Ni_3(HITP)_2$ provides extra channels for electron transport, while its microporous structure exhibits strong reflection and phonon scattering capabilities. Therefore, the $Ni_3(HITP)_2$@fiber film possesses considerable electrical conductivity and low thermal conductivity, acting as a photo-thermoelectric generator with a Seebeck coefficient of –23.7 μV K^{-1}. Coupled with the high photoabsorption and low thermal expansion of $Ni_3(HITP)_2$, the $Ni_3(HITP)_2$@fiber/polymer actuator exhibits bending actuation and concurrently outputs self-powered sensing signals under sunlight irradiation. An intelligent window system with sensing and feedback functions based on the actuators is designed for intelligent home. Additionally, an intelligent gripper system with sensing, feedback, and indication functions is constructed. The operating states of the gripper, self-powered signals, and indicating colors of light-emitting diodes are highly synchronized. This actuator offers great potential for applications in intelligent home and Industry 4.0.

1. Introduction

Actuating materials, which efficiently convert external controllable stimuli (e.g., light [1,2], heat [3], electricity [4], magnetism [5], and humidity [6]) into mechanical energy, have garnered significant interest in fields such as soft robotics, biomedicine, and bionic systems [7–11]. However, with the advancement of Internet of Things (IoT) technology and the increasing reliance on electronic devices across various sectors, there is an urgent need to develop smart actuators that can simultaneously provide power and sense key parameters. These devices enable autonomous operation and intelligent sensing [12,13]. Compared to the traditional approach of combining multiple devices, the development of integrated, self-powered actuators with sensing capabilities is an ideal solution, as they require no external power supply and have low energy consumption.

Solar energy, as a renewable and eco-friendly source, can be captured anywhere [14–16]. Compared to humidity-driven and electricity-driven methods, the sunlight-driven actuator incorporates the advantages of wireless driving, remote operation and precise control (Table S1). Therefore, the development of solar energy and its

* Corresponding authors.
E-mail addresses: gewang@fjirsm.ac.cn (G.-E. Wang), ChenLZ@fjnu.edu.cn (L. Chen).
[1] These authors contributed equally to this work.

https://doi.org/10.1016/j.cej.2025.162835
Received 7 January 2025; Received in revised form 25 March 2025; Accepted 18 April 2025
Available online 20 April 2025

application in self-powered actuators have been considered a carbon–neutral approach to alleviate the global energy crisis and environmental pollution. Compared with other types of self-powered modes, self-powered actuators based on the photo-thermoelectric (PTE) effect have attracted great interest from researchers, due to the absence of direct contact, gentle working conditions, easy operation, and efficient conversion efficiencies [17–19]. For instance, Weng et al. developed a multi-responsive bilayer actuator using a graphene cellulose film coated with polypyrrole, which was applied to gesture recognition and self-powered temperature/humidity sensing [20]. Gu et al. designed a light-driven actuator integrated with self-powered/visual dual-mode sensing and rewritable display functions, using a pencil, thermochromic dye, and a polyimide film [21]. Unfortunately, previously reported PTE-based all-in-one actuators typically can only monitor the operating state of the device and output a voltage signal, lacking further utilization of the signal. When environmental conditions change, these devices lack the ability to respond with feedback. The IoT technology enables intelligent interactions between devices through data acquisition and transmission, facilitating real-time monitoring, intelligent control, and remote management [22,23]. Consequently, integration of IoT technology with PTE-based all-in-one actuators is anticipated to support simultaneous monitoring, data transmission and feedback operations in intelligent actuators. Additionally, this integration, which operates without human intervention and autonomously optimizes energy consumption, holds immense potential for applications in smart cities, intelligent homes, and Industry 4.0.

The ZT value, typically used to benchmark the thermoelectric properties of a material, is proportional to the square of the Seebeck coefficient and inversely proportional to the thermal conductivity [24,25]. Therefore, the thermoelectric properties of the materials can be markedly improved by enhancing the Seebeck coefficient and reducing the thermal conductivity. Inorganic thermoelectric materials, such as Bi_2Te_3 and Sb_2Te_3, have demonstrated impressive ZT values [26,27]. However, the inherent brittleness makes them typically showcase poor mechanical durability. Furthermore, rare and environmentally unfriendly elements are required [28]. These disadvantages partly restrict their use. In contrast, organic thermoelectric materials have garnered significant attention in the field of flexible actuators and thermoelectric devices due to their flexibility, cost-effectiveness and eco-friendliness [24,29]. Despite these advantages, the absence of long-range ordering and low charge mobility restrict their thermoelectric performance. Therefore, the design and fabrication of thermoelectric materials necessitate the simultaneous enhancement of electrical conductivity and the reduction of thermal conduction. The introduction of pores into the materials is an effective strategy to improve thermoelectric properties, since pores can strongly scatter phonons [30]. Notably, porosity does not necessarily impede charge transport. Due to the different wavelengths of electrons and phonons, continuous non-porous regions can still provide efficient charge transport pathways [31].

Metal-organic framework (MOF) materials, composed of metal ions bridged with organic ligands, are known for their high porosity, large surface area, and periodically distributed pores with long-range translational symmetry [32–34]. Different from graphene and carbon nanotube with high thermal conductivities [35,36], the microporous structure within the MOF possesses the ability to reflect and scatter phonons, which reduces thermal conductivity [25,37]. In addition, some conductive MOFs (cMOFs) incorporate organic ligands with conjugated π-electron systems or conductive metal coordination centers, which ensure moderate electrical conductivity [31,38]. These advantages render cMOFs ideal materials with high thermoelectric properties. For example, Sun et al. reported a mutually noninterfering flexible pressure–temperature dual-mode sensor based on conductive and microstructured MOF, with great sensitivity and large sensing range [39]. Crucially, the inherent π-π conjugation in cMOFs enhances material stability and mitigates thermal expansion [40]. As a consequence, cMOFs often exhibit lower coefficients of thermal expansion (CTE), which is a significant advantage for photo/thermal-driven actuators that achieve large bending deformations. However, the preparation of large-area flexible cMOF films and the utilization of the advantages of cMOF for PTE-based all-in-one actuators have not been reported.

In this work, we develop a large-area flexible cMOF@fiber composite film by interface-induced growth, referred to as the $Ni_3(HITP)_2$@fiber film, which serves as a self-powered actuator. With the assistance of IoT technology, an actuating system based on the actuators achieves both sensing and feedback functions (Scheme 1**a**). Due to the interaction between hydrophilic sites on $Ni_3(HITP)_2$ and the fibrous substrate, the $Ni_3(HITP)_2$@fiber film exhibits high stability. In consideration of the excellent photothermal properties and low CTE of $Ni_3(HITP)_2$, we laminate the $Ni_3(HITP)_2$@fiber film with a biaxially oriented polypropylene (BOPP) film, forming sunlight-driven actuators with large bending deformations. In addition, synergizing with the considerable electrical conductivity and low thermal conductivity of $Ni_3(HITP)_2$, the $Ni_3(HITP)_2$@fiber film exhibits a Seebeck coefficient of –23.7 μV K^{-1}, surpassing other organic materials such as polyaniline [41], polypyrrole [42], and poly(3,4-ethylenedioxythiophene)(styrenesulfonate) [43], identifying it as an n-type organic thermoelectric material. Importantly, the $Ni_3(HITP)_2$@fiber/BOPP actuator can undergo bending deformation and spontaneously generate thermoelectric signals under simulated sunlight irradiation. Additionally, with the assistance of a program controller, an intelligent window system is constructed with the $Ni_3(HITP)_2$@fiber/BOPP actuator array. This intelligent window can automatically control a mini-fan based on the spontaneously generated PTE signals (Scheme 1b). Finally, an intelligent gripper system is carefully designed to act as a robotic arm. It can not only achieve stable gripping, moving and releasing objects, but also real-time output voltage signals. Simultaneously, with the assistance of a program controller, it automatically controls different colored light-emitting diodes (LEDs) to light up for an indication function (Scheme 1c). Notably, the operating state of the gripper, the voltage signals and the color of the LEDs are highly synchronized. Therefore, this intelligent gripper system achieves comprehensive management of the operating status for the actuator through real-time monitoring, automatic identification and intelligent feedback.

2. Experimental section

2.1. Materials

The commercial fibrous substrate with thickness of 28 μm, which was composed of cellulose paper, and BOPP film with thickness of 30 μm were purchased online. Deionized water was used for all experiments. All solvents and reagents were purchased through commercial suppliers and used without further purification. Nickel chloride hexahydrate, anhydrous ethanol and ammonium hydroxide were purchased from Adamas. 2,3,6,7,10,11-hexaaminotriphenylene hexahydrochloride was synthesized according to the procedure in the previous work [44].

2.2. Preparation of the $Ni_3(HITP)_2$@fiber composite film

Firstly, nickel chloride hexahydrate (6.6 mg) and HITP (2,3,6,7,10,11-hexaaminotriphenylene) (10 mg) were mixed into deionized water (10 mL) and completely dissolved. Secondly, a square fibrous substrate (5 cm × 5 cm) was immersed into the above mixed solution with continuous stirring under air atmosphere. Thirdly, the ammonium hydroxide (400 μL) was added dropwise to the system and the reaction was carried out at 65 °C for 4 h. After the reaction was completed, the formed $Ni_3(HITP)_2$@fiber composite films were washed sequentially with ethanol and deionized water. Finally, the composite films were dried under vacuum at 30 °C. Notably, to ensure that the $Ni_3(HITP)_2$ was uniformly coating on the surface of the fibrous substrate, a secondary growth was carried out.

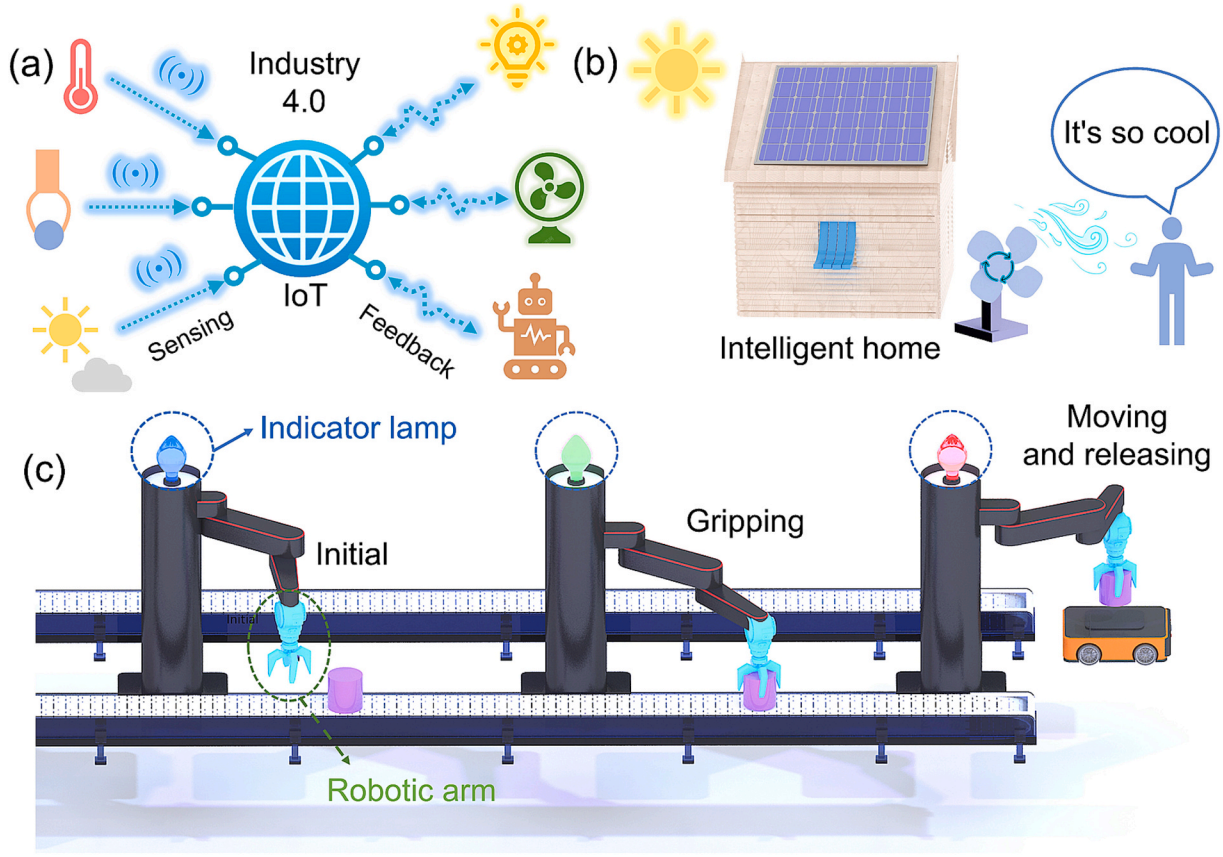

Scheme 1. (a) An all-in-one actuating system with sensing and feedback functions with the assistance of IoT technology. (b) A conceptual diagram of an intelligent window system based on PTE actuator arrays. (c) Intelligent robotic arm with self-powered sensing and indication functions.

2.3. Preparation of the $Ni_3(HITP)_2$@fiber/BOPP actuator

Firstly, the $Ni_3(HITP)_2$@fiber composite film with a thickness of about 36 μm was cut into a strip of 4.5 cm × 0.5 cm. Secondly, a BOPP film with a thickness of about 30 μm was bonded to the prepared $Ni_3(HITP)_2$@fiber film. Finally, the $Ni_3(HITP)_2$@fiber/BOPP actuator was assembled. Notably, the thicknesses of all actuators in subsequent applications are the same.

2.4. Preparation of the $Ni_3(HITP)_2$@fiber/BOPP-based window

Four pre-treated $Ni_3(HITP)_2$@fiber/BOPP actuator units were secured using adhesive tape. Then, the copper electrodes were embedded into each unit with silver adhesive. Finally, the window was assembled by connecting the four actuator units in series.

2.5. Preparation of the intelligent gripper

The intelligent gripper consists of two actuator units. Specifically, the two actuators were attached to the glass slides separately. In particular, the dimension of the free-end portion was 1.5 cm × 0.5 cm. Notably, the portion beyond the free-end of the right actuator was shielded by a photomask to construct the spatial temperature gradient. Then, copper electrodes were embedded into one end of each of the remaining portions of the actuator unit. Finally, the gripper was assembled by attaching these two glass glides with actuator units to the opposite sides of a foam block. The surface of the foam block was brushed with silver adhesive to form a conductive pathway.

2.6. Measurement of PTE properties of the $Ni_3(HITP)_2$@fiber composite film

Firstly, a strip of $Ni_3(HITP)_2$@fiber composite film with the dimensions of 4 cm × 1 cm was attached to a glass frame using polyimide films. Secondly, copper electrodes were embedded at both ends of the strip with silver adhesive. Additionally, a portion (3.5 cm) of the $Ni_3(HITP)_2$@fiber film was shielded with a photomask. Finally, the remaining portion of the $Ni_3(HITP)_2$@fiber film was irradiated with simulated sunlight of different intensities. During this process, the temperature difference and output voltage at both ends of the $Ni_3(HITP)_2$@fiber composite film were recorded by a infrared thermometer and a digital source meter, respectively.

2.7. Measurement of the actuation and PTE properties of $Ni_3(HITP)_2$@fiber/BOPP actuator

First, the $Ni_3(HITP)_2$@fiber/BOPP actuator with dimensions of 4.5 cm × 0.5 cm was attached to a glass slide. In particular, the free-end portion was 1.5 cm × 0.5 cm. The location where the copper electrodes were embedded was provided in the Supporting Information. Afterwards, the portion beyond the free-end of the $Ni_3(HITP)_2$@fiber/BOPP actuator was shielded with a photomask. Finally, the free-end portion of the $Ni_3(HITP)_2$@fiber/BOPP actuator was irradiated with simulated sunlight of different intensities for 5 s, respectively. The real-time temperature difference and output voltage at both ends of the actuator were recorded. Meanwhile, the bending deformation process of the actuator was recorded by a digital camera.

3. Results and discussion

Fig. 1a illustrates the schematic diagram of the fabrication process for the $Ni_3(HITP)_2$@fiber composite film. Specifically, an aqueous solution containing the organic ligand HITP (2,3,6,7,10,11-hexaiminotriphenylene)•6 HCl and nickel (II) chloride hexahydrate was continuously stirred at 65 ℃. Next, a fibrous substrate was immersed in the above reaction mixture. Immediately after, $NH_3{\cdot}H_2O$ was added dropwise into the above mixture. Ultimately, the $Ni_3(HITP)_2$@fiber composite was obtained after 4 h of reaction. During the interface synthesis, the coordination between Ni^{2+} centers and tritopic HITP ligands formed a 2D conjugated structure featuring hexagonal pores within the ab plane. These 2D layers were stacked through strong π-π interactions, resulting in a honeycomb architecture with uniform 1D channels along the c axis (Fig. 1b). More detailed synthesis procedures are provided in the Experimental Section. Additionally, the $Ni_3(HITP)_2$@fiber film was soaked in an aqueous solution for a long time. Notably, no significant shedding of $Ni_3(HITP)_2$ was observed, underscoring the excellent stability of the composites (Fig. S1). This phenomenon was attributed to the fact that the surface of the oxidized fibrous substrate was rich in carboxyl groups, which allowed for the continuous and robust growth of $Ni_3(HITP)_2$ nanolayers (Fig. 1c). Compared to traditional non-conductive MOFs, the $Ni_3(HITP)_2$ possesses unique structural features and electrical properties. First, the arrangement of HITP ligands in

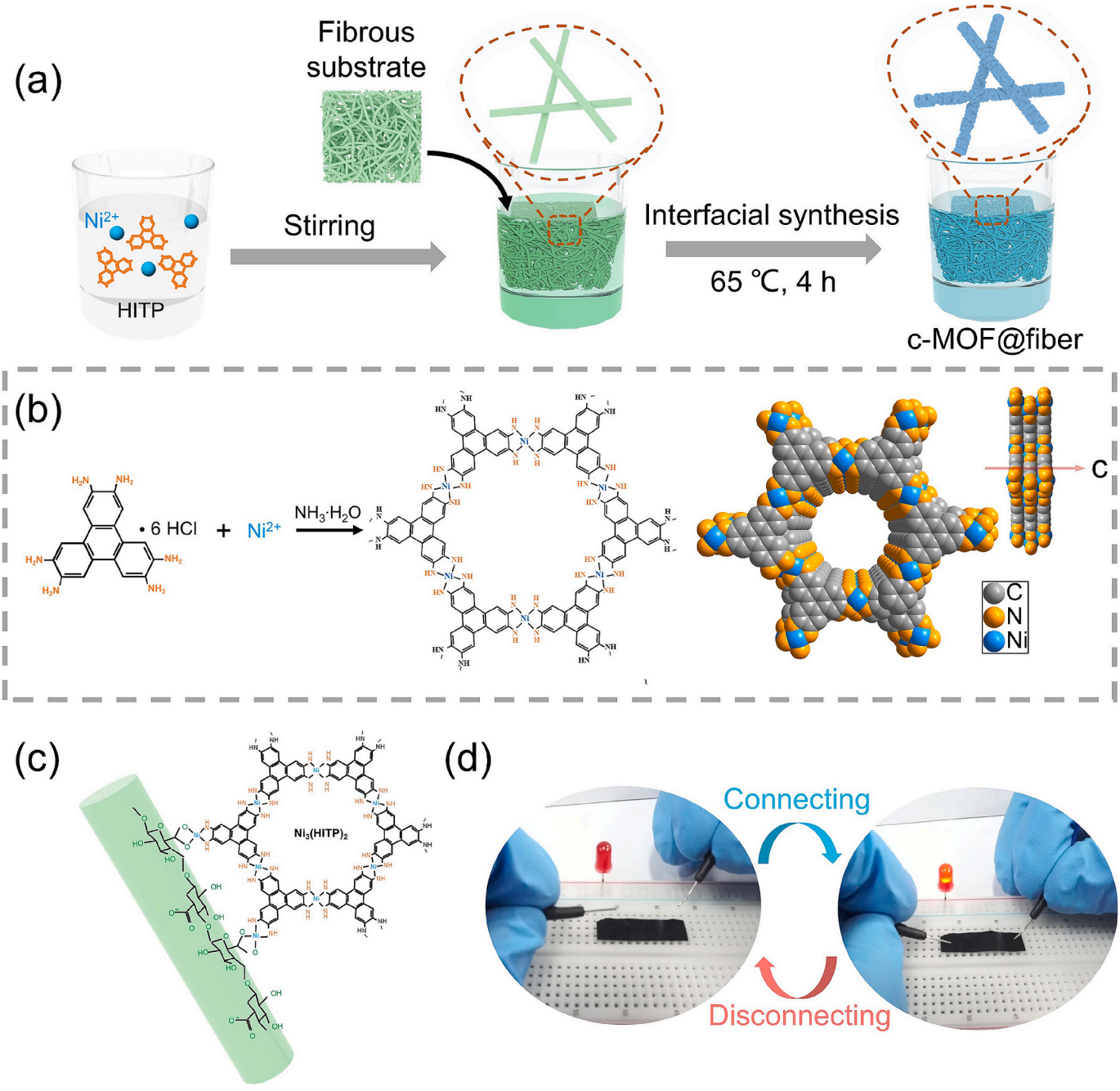

Fig. 1. (a) Schematic illustration of the fabrication process for $Ni_3(HITP)_2$@fiber composites through the interface-induced growth method. (b) Synthesis of $Ni_3(HITP)_2$ and a portion of its crystal structure showing multiple stacked 2D layers. The 2D layered structure gives $Ni_3(HITP)_2$ a uniform 1D pore channel. (c) Molecular structure of $Ni_3(HITP)_2$ layered on the fibrous substrate. (d) Optical photos of the $Ni_3(HITP)_2$@fiber composite film as an electrode material to light a red LED.

$Ni_3(HITP)_2$ forms a continuous π-conjugation network within the entire material, facilitating electron delocalization. Second, the strong π-π conjugation and weak metal–metal interactions in $Ni_3(HITP)_2$ flakes contribute to charge transfer. Third, the unique homogeneous 1D channels of $Ni_3(HITP)_2$ along the c-axis also provide an active path for charge transmission [44]. The electrical conductivity of $Ni_3(HITP)_2$@-fiber composite was measured to be ~ 8.2 S m^{-1} at room temperature (Fig. S2). Fig. 1d demonstrates that the composite film can serve as an electrode material to light a red LED.

The structure and morphology of the pristine fibrous substrate and $Ni_3(HITP)_2$@fiber film can be clearly observed by scanning electron microscopy (SEM) at various scales. As shown in Fig. 2a, the pristine fibrous substrate consists of bundles of fibers with various sizes, intricately interwoven to form a network. Moreover, there are discernible gaps between these fiber bundles (Fig. S3). With the continuous growth of $Ni_3(HITP)_2$ thin film on the fibrous substrate, the $Ni_3(HITP)_2$@fiber film still retains the structural integrity of the pristine fibrous substrate (Fig. 2b). The optical photos in the inset show a clear comparison between the pristine fibrous substrate and the synthetic $Ni_3(HITP)_2$@fiber film. Remarkably, the micrometer-scale macropores of the fibrous substrate still remains in the interior of the $Ni_3(HITP)_2$@fiber film (Fig. 2c). High-magnification SEM image of $Ni_3(HITP)_2$@fiber film further confirms that the fibers are entirely wrapped by continuous $Ni_3(HITP)_2$ nanolayers (Fig. 2d). The cross-sectional SEM image of the pristine fibrous substrate shows that the thickness of the film is about 28 μm (Fig. 2e). In contrast, the thickness of $Ni_3(HITP)_2$@fiber film remains approximately 36 μm (Fig. 2f). Fig. 2g-2j illustrate the SEM image of $Ni_3(HITP)_2$@fiber film and its corresponding elemental mapping. The uniform distribution of C, N, and Ni in the mapping indicates that $Ni_3(HITP)_2$ is uniformly grown on the fibrous substrate.

X-ray diffraction (XRD) patterns of the $Ni_3(HITP)_2$@fiber film and $Ni_3(HITP)_2$ powders were investigated. The characteristic peaks at approximately 4.68°, 9.42°, 12.52°, 16.36° and 27.04° reveal a typical crystalline structure, confirming the successful synthesis of $Ni_3(HITP)_2$ [44]. The N_2 adsorption–desorption isotherm confirms the microporous characteristics of $Ni_3(HITP)_2$. In particular, the pore size distribution of $Ni_3(HITP)_2$ is concentrated at 1.5 nm (Fig. S4). Moreover, the prominent peak positions of $Ni_3(HITP)_2$@fiber film coincide with the above results, indicating the successful growth of $Ni_3(HITP)_2$ on the fibrous substrate (Fig. 3a). Raman spectra were investigated to characterize the $Ni_3(HITP)_2$ and $Ni_3(HITP)_2$@fiber composites, as shown in Fig. 3b. The two characteristic peaks at 1,365 cm^{-1} and 1,563 cm^{-1} are assigned to the breathing mode of the κ-point phonon at the D-band and the E_{2g} phonon of the sp^2 C atoms at the G-band, respectively [45]. Furthermore, to assess the effect of induced growth of $Ni_3(HITP)_2$ on the photothermal properties of the material, the UV–vis-NIR absorption spectra of the fibrous substrate before and after the growth of $Ni_3(HITP)_2$ were measured (Fig. 3c). The results indicate that the photoabsorption of the pristine fibrous substrate is poor, with an average absorption of approximately 20 % in the wavelength range of 250–2500 nm. There is a slight rise beyond 1870 nm. In contrast, the $Ni_3(HITP)_2$@fiber film overall exhibits strong photoabsorption, with an average photoabsorption of approximately 80 %, encompassing the full solar spectrum. In particular, the photoabsorption of the $Ni_3(HITP)_2$@fiber film exceeds 85 % in the wavelength range of 250–870 nm. Meanwhile, the photoabsorption decreases over 2000 nm. Moreover, according to

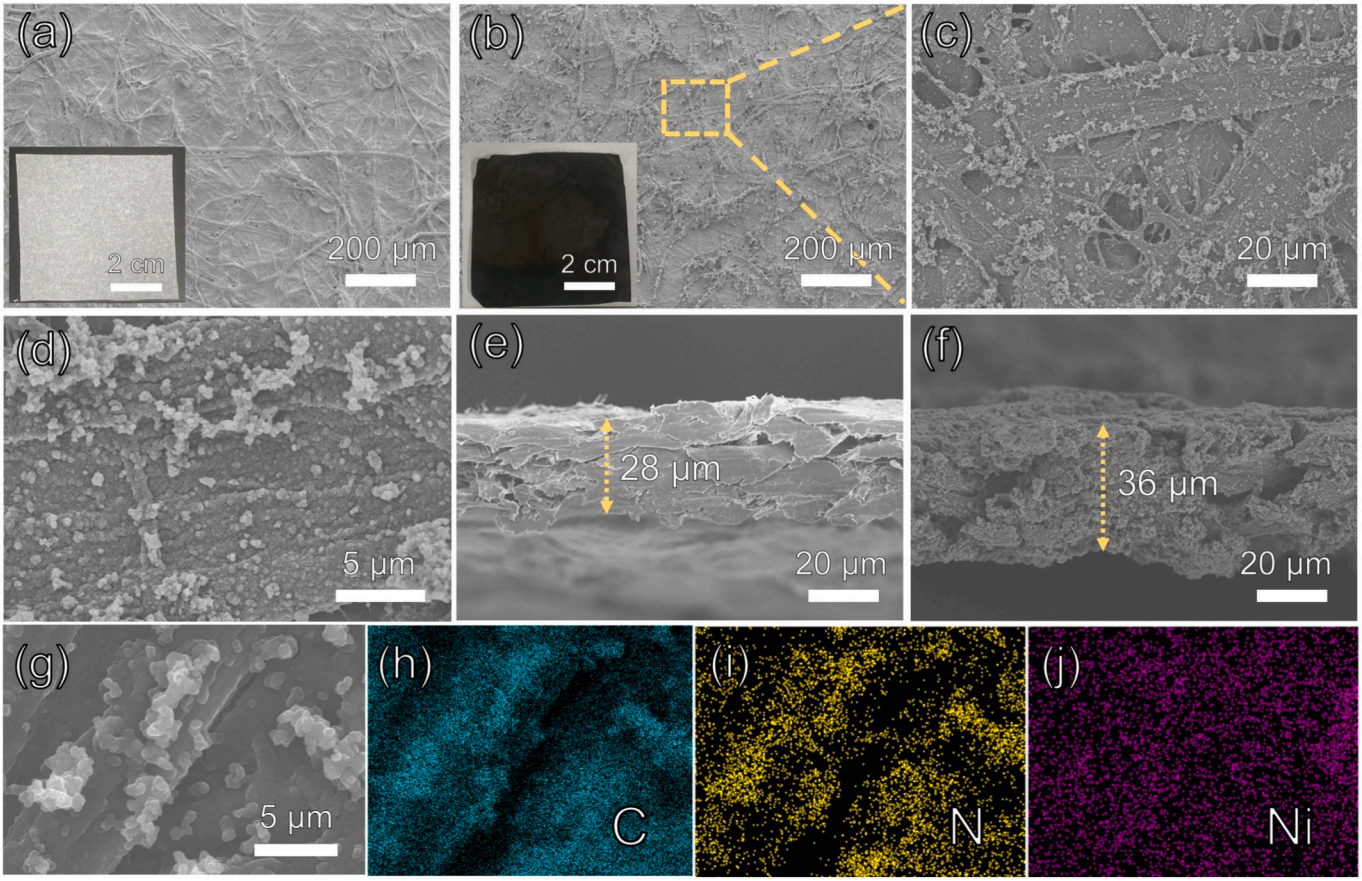

Fig. 2. (a) Surface SEM image of the pristine fibrous substrate. The inset shows an optical photograph of the pristine fibrous substrate. (b) Surface SEM image of the $Ni_3(HITP)_2$@fiber film. The inset shows an optical photograph of the $Ni_3(HITP)_2$@fiber film. (c) Medium-magnification SEM image of $Ni_3(HITP)_2$@fiber film. (d) High-magnification SEM image of $Ni_3(HITP)_2$@fiber film. (e) Cross-sectional SEM image of the pristine fibrous substrate. (f) Cross-sectional SEM image of the $Ni_3(HITP)_2$@fiber film. (g) SEM image of $Ni_3(HITP)_2$@fiber film and its corresponding elemental mapping images for (h) C, (i) N and (j) Ni.

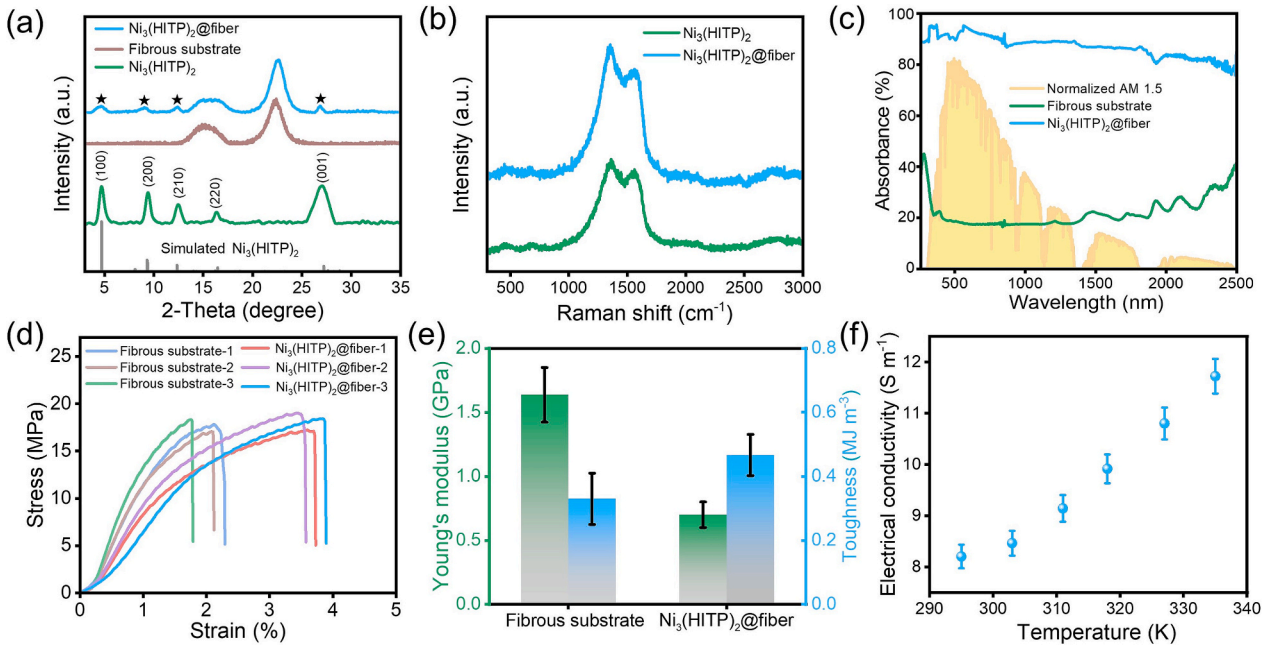

Fig. 3. (a) XRD patterns of fibrous substrate, $Ni_3(HITP)_2$ and $Ni_3(HITP)_2$@fiber composite. (b) Raman spectra of $Ni_3(HITP)_2$ and $Ni_3(HITP)_2$@fiber composite. (c) UV–vis-NIR absorption spectra of the pristine fibrous substrate, $Ni_3(HITP)_2$@fiber film and AM 1.5 standard spectrum. (d) Tensile stress–strain curves of the pristine fibrous substrate and $Ni_3(HITP)_2$@fiber film. (e) Young's modulus and toughness of the pristine fibrous substrate and $Ni_3(HITP)_2$@fiber film. (f) Electrical conductivity of $Ni_3(HITP)_2$@fiber films under different temperatures.

Fourier's law [40,46], the thermal conductivity of the $Ni_3(HITP)_2$@fiber composite film was estimated to be less than that of standard A4 printing paper (0.05 W m^{-1} K^{-1}) (Fig. S5). The excellent photoabsorption and low thermal conductivity of $Ni_3(HITP)_2$@fiber film assist in coupling the photothermal and thermoelectric effects to generate higher output voltages, enhancing the PTE properties.

The mechanical properties of a material are important parameters in its practical application. Several tensile experiments were conducted on the pristine fibrous substrate and $Ni_3(HITP)_2$@fiber film. As shown in Fig. 3d, the pristine fibrous substrate displays an average tensile strength of 17.9 MPa and an average breaking strain of 2.1 %. In contrast, the $Ni_3(HITP)_2$@fiber film shows an average tensile strength of 18.4 MPa and an average breaking strain of 3.7 %. In addition, the Young's modulus of fibrous substrate decreased from 1.64 to 0.70 GPa after

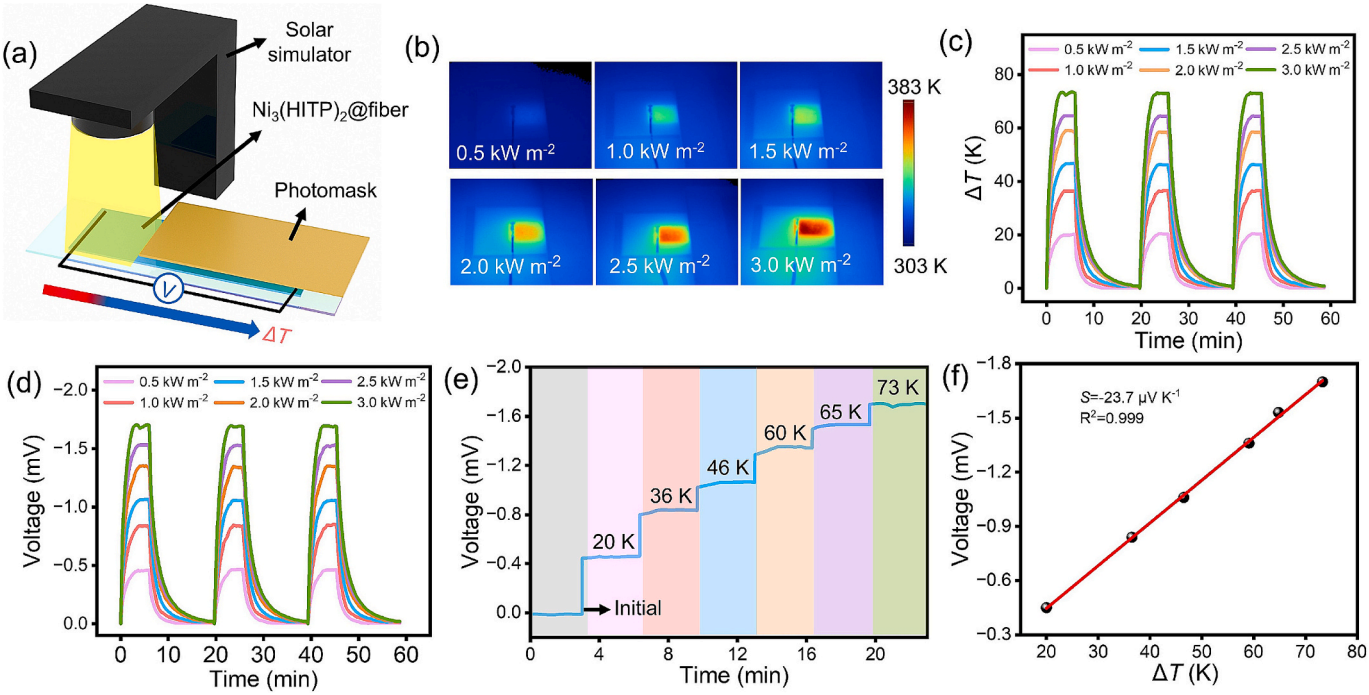

Fig. 4. (a) Schematic illustration of a prototype for the photo-thermoelectric property test. (b) Infrared images of $Ni_3(HITP)_2$@fiber film under different solar intensities. (c) Cyclic response of ΔT for $Ni_3(HITP)_2$@fiber film under different solar intensities. (d) Cyclic response of output voltage of $Ni_3(HITP)_2$@fiber film under different solar intensities. (e) Stepped change of output voltage with increasing ΔT. (f) Output voltage of the $Ni_3(HITP)_2$@fiber film as a function of ΔT.

surface-induced growth of $Ni_3(HITP)_2$, while the toughness increased from 0.33 to 0.47 MJ m^{-3} (Fig. 3e). These results demonstrate that the toughness of composites can be enhanced by the growth of $Ni_3(HITP)_2$ on the fibrous surface, with almost no change in the tensile strength. The above characteristics are advantageous for practical use and storage. Additionally, the electrical properties of $Ni_3(HITP)_2$@fiber film under different temperatures were investigated (Fig. S6). As shown in Fig. 3f, the electrical conductivity of $Ni_3(HITP)_2$@fiber film increased with increasing temperature. Specifically, when the temperature was increased from 295 K to 335 K, the conductivity of the $Ni_3(HITP)_2$@fiber film was improved from 8.2 S m^{-1} to 11.7 S m^{-1}.

A prototype was designed to systematically investigate the PTE properties of $Ni_3(HITP)_2$@fiber film (Fig. 4a, Fig. S7). One end (1 cm × 1 cm) of the $Ni_3(HITP)_2$@fiber film was irradiated by a xenon lamp, referred to as the solar simulator. The other end (3.5 cm × 1 cm) was shielded by a photomask. Owing to the photothermal effect, the temperature increased rapidly at the irradiated end. In contrast, the temperature at the other end remained almost unaltered. This phenomenon was mainly attributed to the low thermal conductivity of $Ni_3(HITP)_2$. The temperature distribution of $Ni_3(HITP)_2$@fiber film under a solar intensity of 2 kW m^{-2} was recorded (Fig. S8). The results demonstrate that there was no significant thermal diffusion between the hot and cold ends of the $Ni_3(HITP)_2$@fiber film. The temperature difference (ΔT) reached 25 K for a distance of 2 cm. Notably, the temperature at the cold-end was almost unchanged. The infrared images of $Ni_3(HITP)_2$@-fiber film under different solar intensities are provided in Fig. 4b. With the increase of solar intensity, the hot-end temperature of $Ni_3(HITP)_2$@fiber film gradually rises and is uniformly distributed. Obviously, the $Ni_3(HITP)_2$@fiber film accurately responds to external solar intensity changes, showing excellent reproducibility and recognizability (Fig. 4c). In particular, the PTE effect of $Ni_3(HITP)_2$@fiber enables the composite film to possess excellent self-powered capability. Fig. 4d illustrates the dynamic open-circuit voltage under different solar intensities. Six temperature gradients were applied to both ends of $Ni_3(HITP)_2$@fiber film under different intensities of simulated sunlight. The open-circuit voltages were obtained (Fig. 4e). Specifically, the open-circuit voltage was up to −1.71 mV at a ΔT of 73 K. As shown in Fig. 4f, the thermoelectric output voltage of $Ni_3(HITP)_2$@fiber film increases with ΔT, and the voltage-ΔT curve exhibits a strong linear relationship in the temperature range of ΔT from 20 K to 73 K. Consequently, the slope of the voltage-ΔT curve, namely Seebeck coefficient (S), is calculated to be –23.7 μV K^{-1}. The performance of the $Ni_3(HITP)_2$@fiber film is at the medium–high level among previously reported single flexible thermoelectric materials (Table S2).

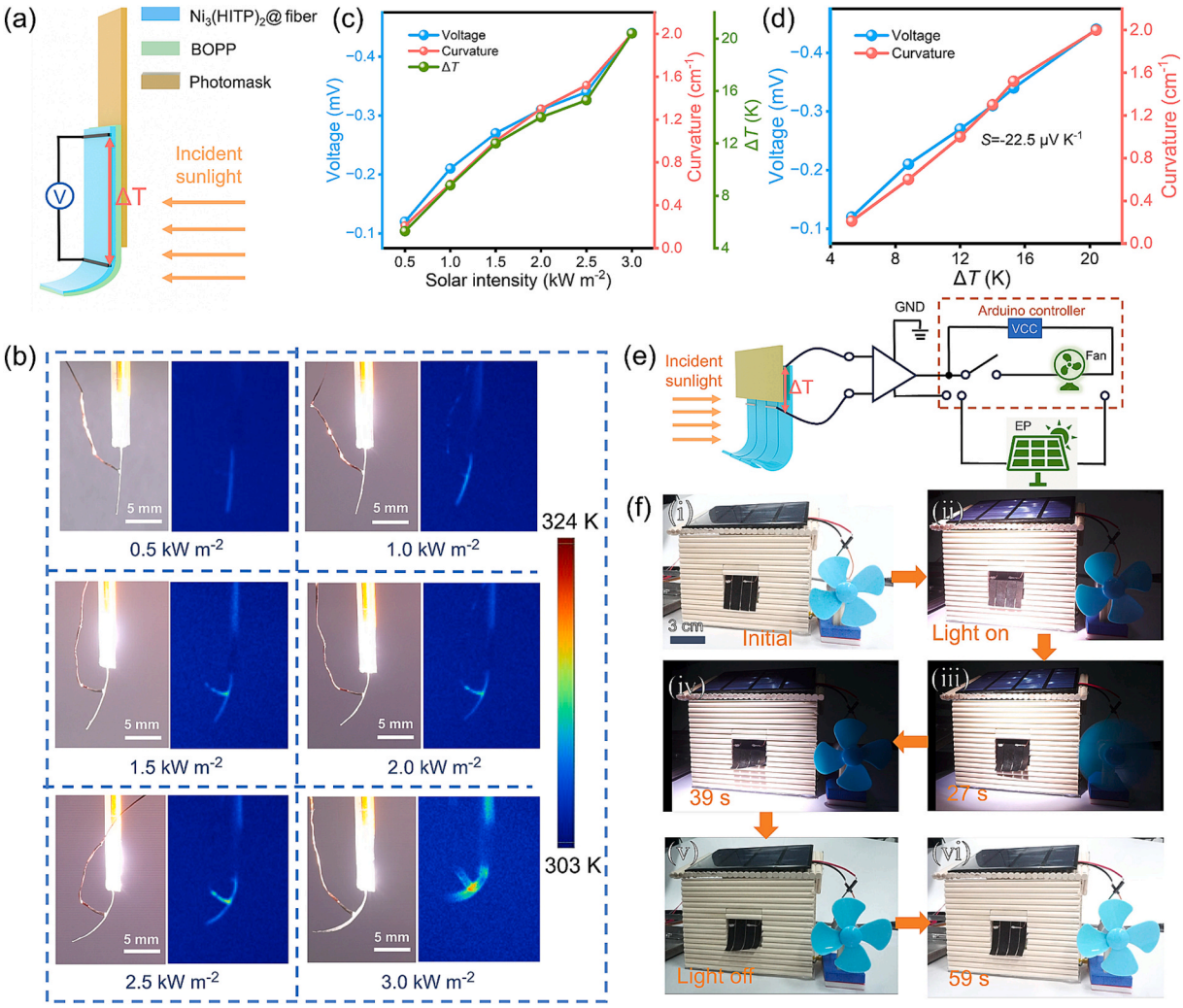

Fig. 5. (a) Schematic diagram of a prototype sunlight-driven actuator with self-powered sensing function. (b) Optical photographs and the infrared images of the maximum bending amplitude of $Ni_3(HITP)_2$@fiber/BOPP actuator under different solar intensities. (c) Maximum ΔT, bending curvature and output voltage of $Ni_3(HITP)_2$@fiber/BOPP actuator as a function of solar intensity. (d) Maximum output voltage and bending curvature of $Ni_3(HITP)_2$@fiber/BOPP actuator as a function of ΔT. (e) Schematic diagram of the principle of the intelligent window system. (f) Optical photographs of the intelligent window system at different stages. (i) Initial, (ii) light on, (iii) light on for 27 s, (iv) light on for 39 s, (v) light off, (vi) after 59 s.

The conflict between rigid MOFs and flexible substrates was addressed by induced growth of $Ni_3(HITP)_2$ thin film on fibrous substrate, while simultaneously optimizing the mechanical and photothermal properties of the composites. Moreover, in consideration of the excellent PTE properties of $Ni_3(HITP)_2$@fiber film, a sunlight-driven actuator was fabricated by combining the $Ni_3(HITP)_2$@fiber film with a BOPP film. The device was expected to undergo mechanical deformation, while generating self-powered thermoelectric sensing signals. As shown in Fig. 5a, a section (3 cm) of a rectangular $Ni_3(HITP)_2$@fiber/BOPP actuator was fixed on a glass slide. Meanwhile, the remaining section (1 cm) of the actuator could bent freely to deform under simulated solar irradiation. Furthermore, to construct a spatial temperature gradient at both ends of the $Ni_3(HITP)_2$@fiber/BOPP actuator, a copper foil affixed with the other side of the glass slide, referred to as a photomask. At the same time, copper electrodes were affixed to the cold-end terminus and 1 cm from hot-end terminus of the $Ni_3(HITP)_2$@fiber/BOPP actuator, respectively, with silver adhesive (Fig. S9). When the simulated sunlight irradiated the $Ni_3(HITP)_2$@fiber/BOPP actuator, the free-end of the actuator bent. Moreover, due to the PTE effect, an output voltage signal was generated spontaneously at both ends of the $Ni_3(HITP)_2$@fiber/BOPP actuator.

Optical photographs and infrared images of the $Ni_3(HITP)_2$@fiber/BOPP actuator were recorded during sunlight irradiations (0.5 kW m^{-2} to 3.0 kW m^{-2}) for 5 s (Fig. 5b, Fig. S10). The results reveal that the bending deformation and surface temperature of the $Ni_3(HITP)_2$@fiber/BOPP actuator gradually increase with the enhancement of simulated sunlight intensity. The response time and recovery time of the actuator under different solar intensities are provided in Table S3. Obviously, the higher the solar intensity, the more energy absorbed by the actuator and the shorter the response time. In contrast, the actuator takes longer time to recover due to the water absorption process. This actuation mechanism of the sunlight-driven actuator is mainly attributed to the asymmetric thermal expansion effect of $Ni_3(HITP)_2$@fiber film and BOPP film. Specifically, the inherent π-π conjugation effect of $Ni_3(HITP)_2$ restricts the thermal expansion motion within itself, typically showing a low CTE [40]. The CTE of the fibrous substrate is in the range of 4–16 ppm K^{-1} [47]. In contrast, the CTE of BOPP is 137 ppm K^{-1} [48]. When the simulated sunlight irradiated the $Ni_3(HITP)_2$@fiber/BOPP actuator, due to the mismatch in volume change caused by the differences of CTE between the bilayer structures, it ultimately bent towards the $Ni_3(HITP)_2$@fiber side. Fig. 5c shows the maximum values of the ΔT, bending curvature and output voltage of $Ni_3(HITP)_2$@fiber/BOPP actuator under different solar intensities. The ΔT, bending curvature and output voltage remain synchronized with increasing solar intensities. The maximum values of ΔT, output voltage and bending curvature of the $Ni_3(HITP)_2$@fiber/BOPP actuator are 20.4 K, −0.44 mV and 2.0 cm^{-1}, respectively, at a solar intensity of 3 kW m^{-2}. The calculation details of the bending curvature of the actuator are provided in Supplementary Note 1 and Fig. S11. The fitted Seebeck coefficient for the $Ni_3(HITP)_2$@fiber/BOPP actuator is –22.5 μV K^{-1} (Fig. 5d). This result is similar to that of the previous PTE property tests. These findings indicate that the sunlight-driven deformation and the PTE signals of this $Ni_3(HITP)_2$@fiber/BOPP actuator are mutually non-interfering, which is a significant advantage for practical use. At the same time, the actuator has a high matching relationship between the self-powered voltage and the bending curvature (matching rate of more than 99 %). The excellent synchronization characteristics of the $Ni_3(HITP)_2$@fiber/BOPP actuator enable the temperature and the deformation amplitude to be observed in real-time by monitoring the self-powered output voltage.

Based on this $Ni_3(HITP)_2$@fiber/BOPP actuator with self-powered sensing function, a prototype of all-solar-powered intelligent window system was constructed to implement carbon neutrality. Specific dimensions of the window are provided in Fig. S12. The operation principle of this intelligent window is shown in Fig. 5e. First, an array composed of four actuator units was constructed to act as a window. Second, one end of this window was irradiated by simulated sunlight. In contrast, the other end was shielded with a photomask. Then, the window was opened automatically, and the output voltage signals were generated spontaneously at both ends. Afterwards, this output voltage was amplified by a signal amplifier and introduced into a program controller. Notably, an Arduino development board served as the program controller (Fig. S13). As the window was continuously irradiated by simulated sunlight, the output voltage signals were gradually enhanced. Once the output voltage reached a preset threshold, the switch on the program controller closed, making the mini-fan operate (Video S1). Meanwhile, a solar battery panel served as the external power (EP). In contrast, the internal power of the program controller, i.e., the voltage common collector (VCC, 5 V), was typically used to power the circuit components. Fig. 5f exhibits optical photographs of the intelligent window system at different stages. Initially, the window was closed and the mini-fan did not work (Fig. 5f-i). When the simulated sunlight was turned on, the window was gradually opened. Since the output voltage was low at this time, the switch of the program controller remained disconnected. Therefore, the mini-fan still did not work (Fig. 5f-ii). After the simulated sunlight was turned on for a while, the window was opened more obviously and the output voltage increased. When the intelligent window was irradiated by the simulated sunlight for 27 s, the mini-fan started to work (Fig. 5f-iii). After 36 s, since the incident simulated sunlight deviated from its initial position, the output voltage started to decrease. The mini-fan stopped working at 39 s, as the output voltage fell below the threshold value (Fig. 5f-iv). After the simulated sunlight was turned off, the intelligent window rapidly closed (Fig. 5f-v). Finally, the intelligent window gradually returned to the initial state after 59 s (Fig. 5f-vi). The real-time output voltage signals of this intelligent window system are provided in Fig. S14.

The $Ni_3(HITP)_2$@fiber/BOPP actuator maintains remarkably high synchronization between the sunlight-driven shape-deformation and the spontaneous output voltage signals, and the $Ni_3(HITP)_2$@fiber composite film possesses good electrical conductivity. Combining these features, a prototype of intelligent gripper integrated with sensing and indication functions was designed. The principal schematic of the intelligent gripper is shown in Fig. 6a, consisting of two strips of $Ni_3(HITP)_2$@fiber/BOPP actuator. Schematic dimension of the intelligent gripper is shown in Fig. S15. When irradiated by simulated sunlight, the actuators on both sides bent, triggering the circuit. Due to the spatial temperature gradient at both ends of the gripper, the output voltage signal was spontaneously generated. This voltage was amplified and introduced into the program controller. Then, the blue, green, and red LEDs were lighted up sequentially. Fig. 6b displays the output voltage signals of the intelligent gripper at different stages. Initially, without simulated sunlight irradiation, the gripper remained opened, and there was no output voltage signal (Fig. 6c-i). At this stage, channel 1 was connected. Once the simulated sunlight was turned on, the gripper gradually closed until it grasped the object (Fig. 6c-ii), and the voltage signals at both ends began to rise. However, due to the limited voltage, only the blue LED was lighted up. As the simulated sunlight irradiation time increased, the gripper tightened its hold on the object, and the voltage continued to rise until it reached level 1. At this point, channel 1 was disconnected, and channel 2 was connected, lighting the green LED (Fig. 6c-iii). Then, the gripper lifted, moved, and put down the object. During this process, the output voltage kept increasing. Impressively, the weight of the object gripped by the intelligent gripper was approximately six times heavier than that of the free portion of the two $Ni_3(HITP)_2$@fiber/BOPP actuators. When the voltage increased to level 2, channel 2 was disconnected, while channel 3 was connected, lighting the red LED (Fig. 6c-iv). When the simulated sunlight was turned off, the thermoelectric voltage gradually decreased, and the gripper slowly reverted to its initial state (Fig. 6c-v). As the voltage dropped below level 2, channel 3 was disconnected, and channel 2 was reconnected, lighting the green LED (Fig. 6c-vi). When the voltage decreased below level 1, the channel 2 was disconnected, and channel 1 was reconnected, lighting the blue LED (Fig. 6c-vii). As the gripper gradually opened, the

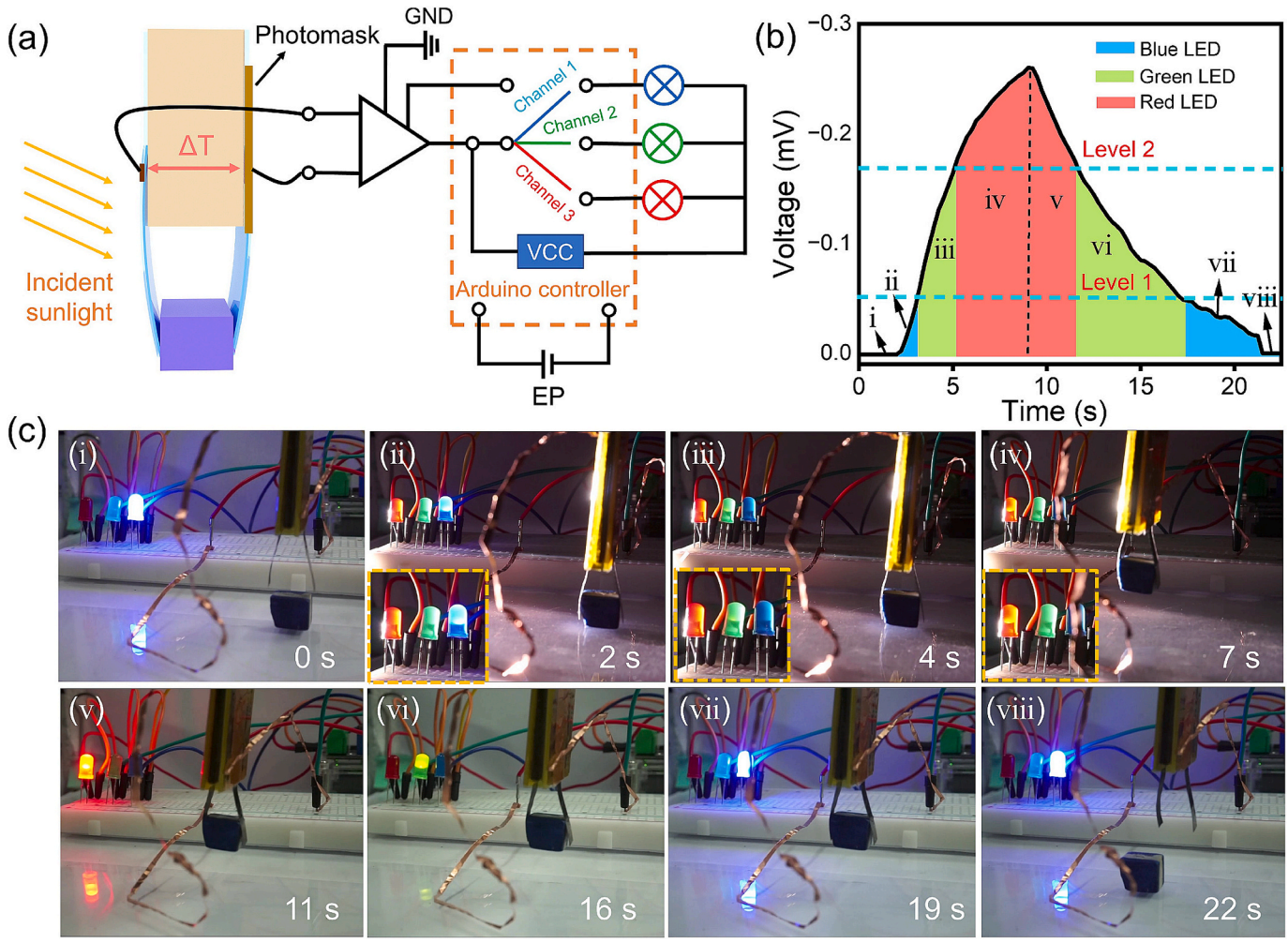

Fig. 6. (a) Schematic illustration of the principle of the intelligent gripper system. (b) Output voltage signals for the intelligent gripper as a function of time. (c) Optical photographs of the intelligent gripper during the process of grasping, moving and releasing an object.

object was released (Fig. 6c-viii), and the output voltage returned to its initial state. The complete demonstration is available in Video S2.

Impressively, the working state, output voltage, and illuminated LED color for the intelligent gripper system are all well-correlated. Therefore, this intelligent gripper not only features thermoelectric sensing capabilities, but also can monitor its operational status via the LED colors. This characteristic is advantageous for future intelligent robotic arm applications.

4. Conclusion

In summary, a conductive $Ni_3(HITP)_2$ thin film is successfully synthesized and induced to grow on a flexible fibrous substrate to obtain large-area $Ni_3(HITP)_2$@fiber composite film. Synchronized with its considerable electrical conductivity and low thermal conductivity, the composite film showcases superior thermoelectric properties, surpassing those of other pure organic materials. Additionally, due to the inherent high photoabsorption and low CTE of $Ni_3(HITP)_2$, the self-powered $Ni_3(HITP)_2$@fiber/BOPP actuator displays large bending deformation under simulated sunlight irradiation. Impressively, automatic bending deformation of the actuator correlates highly with the output PTE signals. With the assistance of IoT technology, an intelligent window system with sensing and feedback functions is elaborately designed for the smart home system. When the outdoor temperature is high, the intelligent window opens automatically. Simultaneously, it can also intelligently control a mini-fan by recognizing the voltage signals. Furthermore, a prototype of intelligent gripper system is constructed based on this all-in-one self-powered actuator. The intelligent gripper can not only grasp and release objects, but also can synchronously output voltage signals. Interestingly, the gripper identifies the voltage signals by a programmable controller, which turns on different colored LEDs to indicate the operating status of the gripper. This research is expected to provide valuable insights to the development of self-powered, all-in-one and highly intelligent bionic devices for practical use.

CRediT authorship contribution statement

Yongqiang Qian: Writing – original draft, Investigation, Funding acquisition, Formal analysis, Data curation. **Wanyi Cheng:** Validation, Software, Investigation, Data curation. **Gang Xu:** Writing – review & editing, Funding acquisition. **Guan-E Wang:** Writing – review & editing, Investigation, Funding acquisition. **Luzhuo Chen:** Writing – review & editing, Supervision, Resources, Funding acquisition, Conceptualization.

Declaration of competing interest

The authors declare that they have no known competing financial interests or personal relationships that could have appeared to influence the work reported in this paper.

Acknowledgements

This work is supported by National Natural Science Foundation of China [grant numbers 52373113, 22422508, 22325109, 22271281], Natural Science Foundation of Fujian Province [grant number 2022J06032], Self-deployment Project Research Program of Haixi Institutes, Chinese Academy of Sciences [grant numbers CXZX-2022-JQ03, CXZX-2022-GH09], Top Young Talents Program of Fujian Province, Startup Fund for Advanced Talents of Putian University [grant number 2024040].

Appendix A. Supplementary material

Supplementary data to this article can be found online at https://doi.org/10.1016/j.cej.2025.162835.

Data availability

Data will be made available upon reasonable request.

References

[1] J. Deng, J. Li, P. Chen, X. Fang, X. Sun, Y. Jiang, W. Weng, B. Wang, H. Peng, Tunable photothermal actuators based on a pre-programmed aligned nanostructure, J. Am. Chem. Soc. 138 (2016) 225–230.
[2] P. Zhang, G. Wang, H. Yu, Ultraviolet-visible-near-infrared light-responsive soft materials: fabrication, photomechanical deformation and applications, Responsive Mater. 2 (2024) e20240016.
[3] J. Li, L. Mou, Z. Liu, X. Zhou, Y. Chen, Oscillating light engine realized by photothermal solvent evaporation, Nat. Commun. 13 (2022) 5621.
[4] S. Chen, S.F. Tan, H. Singh, L. Liu, M. Etienne, P.S. Lee, Functionalized MXene films with substantially improved low-voltage actuation, Adv. Mater. 36 (2024) 2307045.
[5] Y. Lee, F. Koehler, T. Dillon, G. Loke, Y. Kim, J. Marion, M. Antonini, I.C. Garwood, A. Sahasrabudhe, K. Nagao, X. Zhao, Y. Fink, E.T. Roche, P. Anikeeva, Magnetically actuated fiber-based soft robots, Adv. Mater. 35 (2023) 2301916.
[6] J. Zhou, Y. Zhang, J. Zhang, D. Zhang, X. Zhou, J. Xiong, Breathable metal-organic framework enhanced humidity-responsive nanofiber actuator with autonomous triboelectric perceptivity, ACS Nano 17 (2023) 17920–17930.
[7] G. Cai, J.H. Ciou, Y. Liu, Y. Jiang, P.S. Lee, Leaf-inspired multiresponsive MXene-based actuator for programmable smart devices, Sci. Adv. 5 (2019) eaaw7956.
[8] M. Ma, L. Guo, D.G. Anderson, R. Langer, Bio-inspired polymer composite actuator and generator driven by water gradients, Science 339 (2013) 186–189.
[9] K. Mishra, N. Devi, S.S. Siwal, Q. Zhang, W.F. Alsanie, F. Scarpa, V.K. Thakur, Ionic liquid-based polymer nanocomposites for sensors, energy, biomedicine, and environmental applications: roadmap to the future, Adv. Sci. 9 (2022) 2202187.
[10] S. Ma, P. Xue, Y. Tang, R. Bi, X. Xu, L. Wang, Q. Li, Responsive soft actuators with MXene nanomaterials, Responsive Mater. 2 (2024) e20230026.
[11] J. Gao, Y. Tang, D. Martella, J. Guo, D.S. Wiersma, Q. Li, Stimuli-responsive photonic actuators for integrated biomimetic and intelligent systems, Responsive Mater. 1 (2023) e20230008.
[12] P. Zhou, J. Lin, W. Zhang, Z. Luo, L. Chen, Photo-thermoelectric generator integrated in graphene-based actuator for self-powered sensing function, Nano Res. 15 (2022) 5376–5383.
[13] Z. Hou, X. Li, X. Zhang, W. Zhang, Z.L. Wang, H. Zhang, A bioinspired, self-powered, flytrap-based sensor and actuator enabled by voltage triggered hydrogel electrodes, Nano Res. 16 (2023) 10198–10205.
[14] Y. Hu, Q. Ji, M. Huang, L. Chang, C. Zhang, G. Wu, B. Zi, N. Bao, W. Chen, Y. Wu, Light-driven self-oscillating actuators with phototactic locomotion based on black phosphorus heterostructure, Angew. Chem. Int. Ed. 60 (2021) 20511–20517.
[15] X. Hao, H. Yao, P. Zhang, Q. Liao, K. Zhu, J. Chang, H. Cheng, J. Yuan, L. Qu, Multifunctional solar water harvester with high transport selectivity and fouling rejection capacity, Nat. Water 1 (2023) 982–991.
[16] Y. Qian, Z. Luo, Y. Wang, W. Zhang, L. Chen, Plant-leaf-inspired MXene-silk composite for intelligent solar steam generation combined with mechanical actuation, Nano Res. 16 (2023) 7792–7800.
[17] Y. Yoon, H. Park, J. Lee, J. Choi, Y. Jung, S. Han, I. Ha, S.H. Ko, Bioinspired untethered soft robot with pumpless phase change soft actuators by bidirectional thermoelectrics, Chem. Eng. J. 451 (2023) 138794.
[18] M. Zadan, D.K. Patel, A.P. Sabelhaus, J. Liao, A. Wertz, L. Yao, C. Majidi, Liquid crystal elastomer with integrated soft thermoelectrics for shape memory actuation and energy harvesting, Adv. Mater. 34 (2022) 2200857.
[19] Z. Tang, P. Cheng, P. Liu, Y. Gao, X. Chen, G. Wang, Tightened 1D/3D carbon heterostructure infiltrating phase change materials for solar-thermoelectric energy harvesting: faster and better, Carbon Energy 5 (2023) e281.
[20] M. Weng, J. Zhou, P. Zhou, R. Shang, M. You, G. Shen, H. Chen, Multi-functional actuators made with biomass-based graphene-polymer films for intelligent gesture recognition and multi-mode self-powered sensing, Adv. Sci. 11 (2024) 2309846.
[21] W. Gu, P. Zhou, W. Zhang, Z. Luo, L. Chen, Pencil-drawn generator built-in actuator for integrated self-powered/visual dual-mode sensing functions and rewritable display, Adv. Sci. 10 (2023) 2206467.
[22] M.A. Ahad, S. Paiva, G. Tripathi, N. Feroz, Enabling technologies and sustainable smart cities, Sust. Cities Soc. 61 (2020) 102301.
[23] H. Wang, M. Han, Y. Song, H. Zhang, Design, manufacturing and applications of wearable triboelectric nanogenerators, Nano Energy 81 (2021) 105627.
[24] M. Burton, G. Howells, J. Atoyo, M. Carnie, Printed thermoelectrics, Adv. Mater. 34 (2022) 2108183.
[25] K.J. Erickson, F. Léonard, V. Stavila, M.E. Foster, C.D. Spataru, R.E. Jones, B. M. Foley, P.E. Hopkins, M.D. Allendorf, A.A. Talin, Thin film thermoelectric metal–organic framework with high seebeck coefficient and low thermal conductivity, Adv. Mater. 27 (2015) 3453–3459.
[26] G. Kim, L. Shao, K. Zhang, K.P. Pipe, Engineered doping of organic semiconductors for enhanced thermoelectric efficiency, Nat. Mater. 12 (2013) 719–723.
[27] Y.S. Jung, D.H. Jeong, S.B. Kang, F. Kim, M.H. Jeong, K. Lee, J.S. Son, J.M. Baik, J. Kim, K.J. Choi, Wearable solar thermoelectric generator driven by unprecedentedly high temperature difference, Nano Energy 40 (2017) 663–672.
[28] L. Sun, B. Liao, D. Sheberla, D. Kraemer, J. Zhou, E.A. Stach, D. Zakharov, V. Stavila, A.A. Talin, Y. Ge, M.D. Allendorf, G. Chen, F. Léonard, M. Dincă, A microporous and naturally nanostructured thermoelectric metal-organic framework with ultralow thermal conductivity, Joule 1 (2017) 168–177.
[29] X. Xu, J. Chen, J. Zhou, B. Li, Thermal conductivity of polymers and their nanocomposites, Adv. Mater. 30 (2018) 1705544.
[30] H. Lee, D. Vashaee, D.Z. Wang, M.S. Dresselhaus, Z.F. Ren, G. Chen, Effects of nanoscale porosity on thermoelectric properties of SiGe, J. Appl. Phys. 107 (2010) 94308.
[31] L. Sun, M.G. Campbell, M. Dincă, Electrically conductive porous metal-organic frameworks, Angew. Chem. Int. Ed. 55 (2016) 3566–3579.
[32] J. Su, S. Yuan, H. Wang, L. Huang, J. Ge, E. Joseph, J. Qin, T. Cagin, J. Zuo, H. Zhou, Redox-switchable breathing behavior in tetrathiafulvalene-based meta-organic frameworks, Nat. Commun. 8 (2017) 2008.
[33] Y. Zang, F. Pei, J. Huang, Z. Fu, G. Xu, X. Fang, Large-area preparation of crack-free crystalline microporous conductive membrane to upgrade high energy lithium-sulfur batteries, Adv. Energy Mater. 8 (2018) 1802052.
[34] C. Wang, H. Zhang, Y. Wang, J. Wu, K.O. Kirlikovali, P. Li, Y. Zhou, O.K. Farha, A general strategy for the synthesis of hierarchically ordered metal-organic frameworks with tunable macro-, meso-, and micro-pores, Small 19 (2023) 2206116.
[35] X. Ruan, Z. Han, Thermal conductivity of monolayer graphene: convergent and lower than diamond, Phys. Rev. B 108 (2023) L121412.
[36] C. Yu, L. Shi, Z. Yao, D. Li, A. Majumdar, Thermal conductance and thermopower of an individual single-wall carbon nanotube, Nano Lett. 5 (2005) 1842–1846.
[37] S. Zhou, V. Apostolopoulou-Kalkavoura, M.V. Tavares Da Costa, L. Bergström, M. Strømme, C. Xu, Elastic aerogels of cellulose nanofibers@metal-organic frameworks for thermal insulation and fire retardancy, Nano-Micro Lett. 12 (2019) 9.
[38] L.S. Xie, G. Skorupskii, M. Dincă, Electrically conductive metal-organic frameworks, Chem. Rev. 120 (2020) 8536–8580.
[39] Y. Li, R. Wang, G. Wang, S. Feng, W. Shi, Y. Cheng, L. Shi, K. Fu, J. Sun, Mutually noninterfering flexible pressure-temperature dual-modal sensors based on conductive metal-organic framework for electronic skin, ACS Nano 16 (2022) 473–484.
[40] S. Zhou, X. Kong, M. Strømme, C. Xu, Efficient solar thermal energy conversion and utilization by a film of conductive metal-organic framework layered on nanocellulose, ACS Mater. Lett. 4 (2022) 1058–1064.
[41] Q. Yao, L. Chen, W. Zhang, S. Liufu, X. Chen, Enhanced thermoelectric performance of single-walled carbon nanotubes/polyaniline hybrid nanocomposites, ACS Nano 4 (2010) 2445–2451.
[42] X. Jin, X. Qi, Y. Wang, J. Yang, H. Li, Z. Zhou, Y. Wang, Polypyrrole/helical carbon nanotube composite with marvelous photothermoelectric performance for longevous and intelligent internet of things application, ACS Appl. Mater. Interfaces 13 (2021) 8808–8822.
[43] D. Yoo, J. Kim, S.H. Lee, W. Cho, H.H. Choi, F.S. Kim, J.H. Kim, Effects of one- and two-dimensional carbon hybridization of PEDOT:PSS on the power factor of polymer thermoelectric energy conversion devices, J. Mater. Chem. A 3 (2015) 6526–6533.
[44] D. Sheberla, L. Sun, M.A. Blood-Forsythe, S. Er, C.R. Wade, C.K. Brozek, A. Aspuru-Guzik, M. Dincă, High electrical conductivity in Ni_3(2,3,6,7,10,11-hexaiminotriphenylene)$_2$, a semiconducting metal-organic graphene analogue, J. Am. Chem. Soc. 136 (2014) 8859–8862.
[45] D. Cai, M. Lu, L. Li, J. Cao, D. Chen, H. Tu, J. Li, W. Han, A highly conductive MOF of graphene analogue $Ni_3(HITP)_2$ as a sulfur host for high-performance lithium-sulfur batteries, Small 15 (2019) 1902605.
[46] H. Ghasemi, G. Ni, A.M. Marconnet, J. Loomis, S. Yerci, N. Miljkovic, G. Chen, Solar steam generation by heat localization, Nat. Commun. 5 (2014) 4449.
[47] Y. Tai, G. Lubineau, Z. Yang, Light-activated rapid-response polyvinylidene-fluoride-based flexible films, Adv. Mater. 28 (2016) 4665–4670.
[48] M. Weng, P. Zhou, L. Chen, L. Zhang, W. Zhang, Z. Huang, C. Liu, S. Fan, Multiresponsive bidirectional bending actuators fabricated by a pencil-on-paper method, Adv. Funct. Mater. 26 (2016) 7244–7253.